

# Tunable-Q contourlet transform for image representation

Haijiang Wang<sup>1,2</sup>, Qinke Yang<sup>3,\*</sup>, Rui Li<sup>1</sup>, and Zhihong Yao<sup>4</sup>

1. Institute of Soil and Water Conservation, Chinese Academy of Sciences and Ministry of Water Resources, Yangling 712100, China;
2. College of Urban and Environment Science, Shanxi Normal University, Linfen 041004, China;
3. College of Urban and Environmental Sciences, Northwest University, Xi'an 710069, China;
4. College of Resources and Environment, North China University of Water Resources and Electric Power, Zhengzhou 450011, China

**Abstract:** A novel tunable-quality-factor (tunable-Q) contourlet transform for geometric image representation is proposed. The Laplacian pyramid in original contourlet decomposes a signal into channels that have the same bandwidth on a logarithmic scale, and is not suitable for images with different behavior in frequency domain. We employ a new tunable-Q decomposition defined in the frequency domain by which one can flexibly tune the bandwidth of decomposition channels. With an acceptable redundancy, this tunable-Q contourlet is also anti-aliasing and its basis is sharply localized in the desired area of frequency and spatial domain. Our experiments in nonlinear approximation and denoising show that the contourlet using a better-suitable quality factor can achieve a more promising performance and often outperform wavelets and the previous contourlets both in visual quality and in terms of peak signal-to-noise ratio.

**Keywords:** contourlet, quality factor (Q-factor), anti-aliasing, multiscale decomposition.

**DOI:** 10.1109/JSEE.2013.00019

## 1. Introduction

Many recent studies showed contourlets as an efficiently directional multiscale image representation scheme, mainly in capturing the intrinsic geometrical structure as a key in visual information [1–9]. Their experiments in many image processing applications showed that the contourlets can significantly outperform some other transforms (e.g., wavelets) both in visual quality and in terms of quality assessment index. However, the previous contourlets should be improved for images of different oscillatory nature.

First and foremost, one should take into account whether the low-quality-factor (low-Q) multiscale pyramid scheme (i.e., the decomposition scheme based on a low-Q

multiscale filter) of the previous contourlets is suitable for images with different behavior in frequency domain. The previous contourlet is constructed as a combination of Laplacian pyramid (LP) and directional filter banks (DFB). The LP as the first stage iteratively decomposes an image into octave frequency bands in frequency domain and can be considered as a constant low-Q transform, i.e., the transform scheme with a constant and low quality factor (Q-factor). This means that high frequency channels have wide bandwidth (BW) and low frequency channels have narrow BW. This scheme or the Q-factor is only suitable for processing less oscillatory signal, but not for relatively more oscillatory signal [10–13]. Images often contain more/less oscillatory features that may cause rich high/low frequency component in the frequency domain, and thus require a tunable-quality-factor (tunable-Q) transform counterpart. However, the LP scheme in the previous contourlet fails to provide such a Q-factor. By improving the LP scheme, in this study, we construct a new tunable-Q contourlet for image representation.

The second improvement is to reduce the aliasing component in the tunable-Q contourlet. We overcome this drawback by directly designing the multiscale filter bank (FB) in frequency domain and reasonably using the cut-off frequency of the FB.

The rest of this paper is structured as follows. We design and discuss the tunable-Q contourlet in Section 2. Then, we show the effectiveness of the tunable-Q as well as the superiority of our contourlet with the experiments in Section 3. The shortcoming of this study and the subsequent tasks in future are summarized in Section 4.

## 2. Tunable-Q contourlet transform

### 2.1 Canceling the aliasing resulted from downsampling

Contourlets outperform wavelets in image representation, but its original version [1] is prone to cause aliasing component outside of desired passband region [14,15]. This

Manuscript received November 17, 2011.

\*Corresponding author.

This work was supported by the National Natural Science Foundation of China (40971173;41071188).

shortcoming could be overcome by the nonsampled contourlet [16]. At the cost of nonsampling, however, this version is impractical due to its computation burden and storage overconsumption. In order to pursue sharply frequency domain localization and acceptable redundancy ratio (Red) as the same time, Lu presented a new contourlet that used a novel multiscale pyramid structure instead of the LP [14]. This version can well reduce the aliasing component in frequency domain and obtain a promising denoising result, compared with the original version. In this section, we will introduce this anti-aliasing employment to our novel tunable-Q contourlet.

Fig. 1 presents the structure of the tunable-Q contourlet, where the I-DFB denotes the inverse transform of the DFB. Similar to the version of Lu, the main idea of our anti-aliasing scheme is to use different FB for the first level and all rest levels, corresponding to different downsampled patterns in these levels. The  $L_i(\omega)$  and  $D_i(\omega)$  ( $i \in \{0, 1\}$ ) in the diagram denote lowpass and highpass filters respectively, with  $\omega = (\omega_1, \omega_2)$ . The highpass branch at the finest scale as well as the bandpass branch at each coarser scale is followed by the DFB. The output of the lowpass filter  $L_0(\omega)$  at the first level is not downsampled, while the outputs of  $L_1(\omega)$  at all rest levels are downsampled along each direction. The key distinction of our employment from that of Lu is the downsampled factor at each downsampled levels. We use a tunable number  $q/p$  ( $p, q \in \mathbf{Z}^+$ ,  $p < q$ , i.e.,  $p/q \in [0, 1]$ ) rather than the fixed number 2 settled by Lu, as showed in Fig. 1. It will be seen that this improvement can really provide us with a tunable-Q multiscale pyramid scheme.

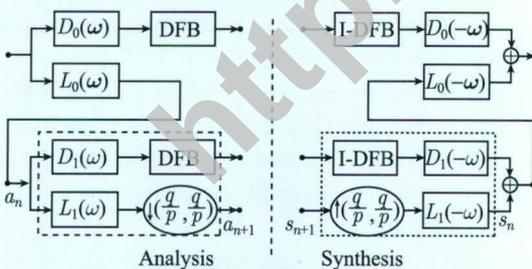


Fig. 1 Structure of the tunable-Q contourlet transform

We design  $L_i(\omega)$  ( $i \in \{0, 1\}$ ) as the tensor product of its one-dimensional (1D) prototype, and  $D_i(\omega)$  in the same way, i.e.,

$$\begin{aligned} L_i(\omega) &= L_i^{1D}(\omega_1)L_i^{1D}(\omega_2), \\ D_i(\omega) &= D_i^{1D}(\omega_1)D_i^{1D}(\omega_2). \end{aligned} \quad (1)$$

In Fig. 1, each downsampler enveloped by an ellipse is a resampler and actually implemented as upsampling by  $p$ , followed an anti-aliasing filter  $R(\omega)$  and then downsampling by  $q$ , as the illustration in Fig. 2.  $R(\omega)$  is an ideal

lowpass filter defined as (2), and  $\omega_{s,i}$  ( $i \in \{0, 1\}$ ) is the stopband-edge frequency of  $L_i^{1D}(\omega)$ .

$$R(\omega) = \begin{cases} 1, & |\omega_1| \leq \omega_{s,0}/q; |\omega_2| \leq \omega_{s,0}/q \\ 0, & \text{otherwise} \end{cases} \quad (2)$$

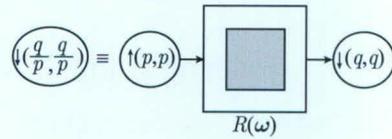
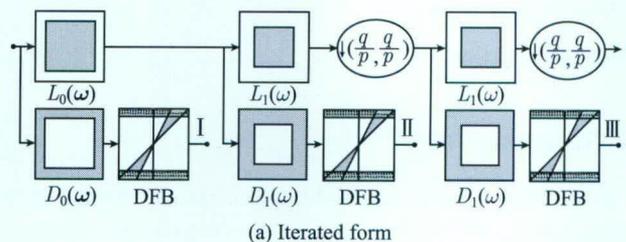
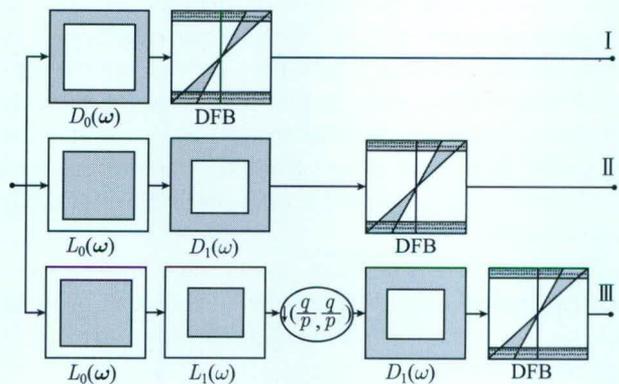


Fig. 2 Ideal sampling rate changer

To demonstrate the aliasing origin from the DFB and the anti-aliasing employment in our new scheme as well, we convert the iterative form of the decompositions in Fig. 1 to its parallel form, and consequently obtain one combined filter for each channel. In Fig. 3(a), we show the block diagram of the decompositions in Fig. 1 in iterative form. There are three levels of radial decomposition, followed by angular decomposition. We display the multiscale decomposition with a simplified and realistic version of its actual implementation, as this version can clearly and exactly illustrate the anti-aliasing employment. Just for the same reason, one of the directional filters in the DFB is chosen here to serve the illustration in stead of the actually whole DFB. The gray regions in the multiscale and directional filters represent the ideal passband support; the gray-dotted regions in the directional filters represent the transition band of the DFB, i.e., the aliasing component



(a) Iterated form



(b) Equivalent parallel form

Fig. 3 Block diagram of the tunable-Q contourlet with three levels of multiscale decomposition

[14]. Fig. 3(b) gives its equivalent parallel form by simply combining the filter block in each channel. Using Noble identity [17] and then combining filter-blocks, we obtain one combined filter for each channel to substitute all

the filters cascaded in this channel. Using this filter and a downsampler which is behind the filter, one can directly gain the highpass output of each decomposition level (I, II, III, in Fig. 3), as shown in Fig. 4.

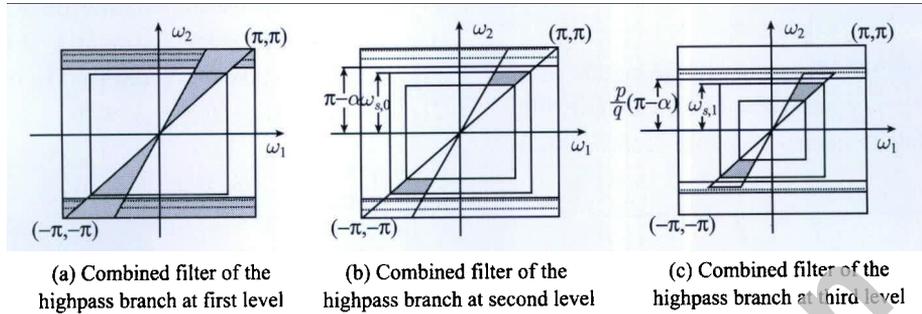


Fig. 4 Illustrations of the anti-aliasing employment in the tunable-Q contourlet

We can pictorially demonstrate the issues above by Fig. 4. It can be seen that the aliasing component from the DFB at the second and the third levels can be completely cancelled out, if the following conditions can be granted,

$$\omega_{s,0} \leq \pi - \alpha, \quad \omega_{s,1} \leq \frac{p}{q}(\pi - \alpha) \quad (3)$$

where  $\alpha$  is the maximum width of the transition band of the DFB. Then, by iteratively using Noble identity, one can infer that the aliasing component at all the subsequent levels can be cancelled under this condition too, and the combined filters at these levels will sharply localize in the desired trapezoid-shaped support area corresponding to a single direction. Therefore, by enforcing the constraint condition (3) in the designing of  $\omega_{s,i}$  ( $i \in \{0, 1\}$ ), as that in this study, the filters at all the levels (only except the first level) can provide us with a desired frequency localization ability.

Based on [14] and [18],  $\alpha$  is specified as  $1/3\pi$ . We have the constraint condition:

$$\omega_{s,0} = \pi - \alpha = \frac{2}{3}\pi, \quad \omega_{s,1} = \frac{p}{q}(\pi - \alpha) = \frac{p}{q} \cdot \frac{2}{3}\pi. \quad (4)$$

## 2.2 Keeping Q-factor constant in multiscale pyramid

In order to achieve a constant-Q multiscale pyramid scheme, the following condition is also considered when designing the multiscale FB.

$$\omega_{s,1} + \omega_{p,1} = \frac{p}{q}(\omega_{s,0} + \omega_{p,0}) \quad (5)$$

where  $\omega_{p,i}$  ( $i \in \{0, 1\}$ ) is the passband edge frequency of  $L_i^{1D}(\omega)$ . Moreover, we also use the constraint condition (6), both for obtaining finer frequency-domain partitions

and specifying the frequency response of the resonant frequency points of these multiscale filters as 1.

$$\omega_{p,0} = \omega_{s,1}. \quad (6)$$

Based on (4), (5) and (6), we have

$$\begin{aligned} \omega_{p,0} = \omega_{s,1} &= \frac{p}{q}\omega_{s,0} = \frac{p}{q} \cdot \frac{2}{3}\pi, \\ \omega_{p,1} = \frac{p}{q}\omega_{p,0} &= \left(\frac{p}{q}\right)^2 \omega_{s,0} = \left(\frac{p}{q}\right)^2 \cdot \frac{2}{3}\pi. \end{aligned} \quad (7)$$

## 2.3 Designing multiscale pyramid FB in frequency domain

We design the filters directly in frequency domain so as to ensure them to be perfectly satisfied with all the conditions above. The 1D prototype  $L_i^{1D}(\omega)$  ( $i \in \{0, 1\}$ ) has ideal passbands and idea stopbands, and smooth passbands as well, defined as (8) inspired by [19].

$$L_i^{1D}(\omega) = \begin{cases} 1, & |\omega| \leq \omega_{p,i} \\ \theta\left(\frac{\omega - a}{b}\right), & \omega_{p,i} \leq |\omega| \leq \omega_{s,i} \\ 0, & \omega_{s,i} \leq |\omega| \leq \pi \end{cases} \quad (8)$$

where  $a = \omega_{p,i}$ ,  $b = \omega_{s,i} - \omega_{p,i}$ , and  $\theta(\omega)$  is such a function defining on  $[0, 1]$  and changing with a certain level of differentiability. We specify the  $\theta(\omega)$  as

$$\theta(\omega) = (1 + \cos(\pi\omega)) \sqrt{2 - \cos(\pi\omega)} / 2, \quad \omega \in [0, 1].$$

Next, we can obtain the  $D_i^{1D}(\omega)$  from  $L_i^{1D}(\omega)$ , based on the perfect reconstruction (PR) condition (9) inferred from the structure in Fig. 1. Then we have (10), where  $\theta_c(\omega)$  is the complementary function of  $\theta(\omega)$ , i.e., there is a relation that  $\theta^2(\omega) + \theta_c^2(\omega) = 1$ .

$$|L_i(\omega)|^2 + |D_i(\omega)|^2 = 1, \quad i \in \{0, 1\}. \quad (9)$$

$$D_i^{1D}(\omega) = \begin{cases} 0, & |\omega| \leq \omega_{p,i} \\ \theta_c \left( \frac{\omega - a}{b} \right), & \omega_{p,i} \leq |\omega| \leq \omega_{s,i} \\ 1, & \omega_{s,i} \leq |\omega| \leq \pi \end{cases} \quad (10)$$

Finally, we obtain the FB in Fig. 1. Taking the case of  $(p, q) = (2, 3)$  (i.e.,  $p = 2$  and  $q = 3$ ) for example, Fig. 5 shows the magnitude frequency response of these filters in their 1D case.

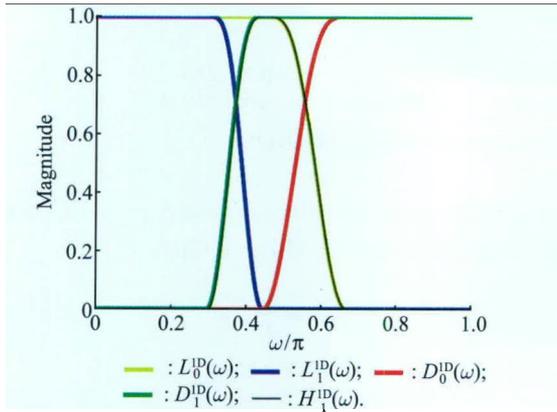


Fig. 5 Frequency response of the FB in Fig. 1 and the combined filter in Section 2.4

### 2.4 Q-factor in multiscale pyramid

For a deeply analysis to the Q-factor of multiscale pyramid filters, we convert the  $n$ -level multiscale decompo-

sition structure in Fig. 1 to its equivalent parallel form again (see Fig. 6), by iteratively exchanging the downsampler with the multiscale filter at every level (as that in Section 2.1, but more completely this time). Here,  $H_j(\omega)$  is the multiscale pyramid filter at level  $j$  ( $j \in \mathbf{Z}$  and  $j \in [0, n]$ ). As  $L_i(\omega)$  and  $D_i(\omega)$  is settled as (1),  $H_j(\omega)$  can also be represented in the same way, i.e.,  $H_j(\omega) = H_j^{1D}(\omega_1)H_j^{1D}(\omega_2)$ , with

$$\begin{cases} H_0^{1D}(\omega) = D_0^{1D}(\omega) \\ H_1^{1D}(\omega) = L_0^{1D}(\omega)D_1^{1D}(\omega) \\ H_2^{1D}(\omega) = L_0^{1D}(\omega)D_1^{1D}\left(\frac{p}{q}\omega\right)L_1^{1D}(\omega) \\ \vdots \\ H_{n-1}^{1D}(\omega) = L_0^{1D}(\omega)D_1^{1D}\left(\left(\frac{p}{q}\right)^{n-2}\omega\right) \times \prod_{k=0}^{n-3} L_1^{1D}\left(\left(\frac{p}{q}\right)^k\omega\right) \\ H_n^{1D} = L_0^{1D}(\omega) \prod_{k=0}^{n-2} L_1^{1D}\left(\left(\frac{p}{q}\right)^k\omega\right) \end{cases} \quad (11)$$

With the case of  $(p, q) = (2, 3)$  again,  $H_1^{1D}(\omega)$  is illustrated in Fig. 7. The central frequency and the BW of  $H_1^{1D}(\omega)$  both decrease gradually, as the decomposition level  $j$  increases. Moreover, we also show the magnitude frequency response of  $H_1^{1D}(\omega)$  in Fig. 5 to pictorially present its relation with  $L_i^{1D}(\omega)$  and  $D_i^{1D}(\omega)$ .

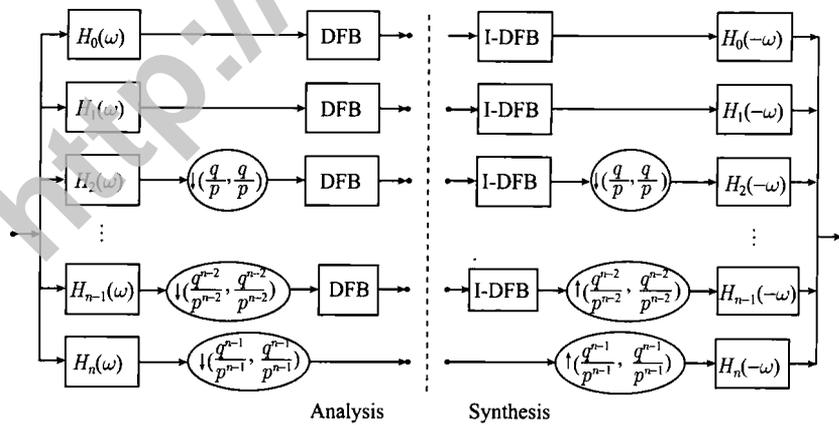


Fig. 6 Equivalent parallel form of the iterated FB in Fig. 1

It can be seen that the aim of this section can be achieved by calculating the Q-factor of  $H_j(\omega)$ . Since  $H_j^{1D}(\omega)$  is the 1D prototype of  $H_j(\omega)$ , the calculation to the Q-factor of  $H_j^{1D}(\omega)$  will obtain the same result as that from  $H_j(\omega)$ . Therefore, we attempt to calculate the Q-factor of the 1D prototype for the sake of simplicity as below.

In the case of  $n$ -level decomposition, the two transition bands of  $H_j^{1D}(\omega)$  ( $0 < j < n$ ) are

$$[\omega_{s,left}, \omega_{p,left}] = \left[ \frac{2}{3} \left( \frac{p}{q} \right)^j \pi, \frac{2}{3} \left( \frac{p}{q} \right)^{j-1} \pi \right],$$

$$\text{and } [\omega_{p,right}, \omega_{s,right}] = \left[ \frac{2}{3} \left( \frac{p}{q} \right)^{j-1} \pi, \frac{2}{3} \left( \frac{p}{q} \right)^{j-2} \pi \right]. \quad (12)$$

where  $\omega_{s,left}$  and  $\omega_{p,left}$  are the stopband edge frequency

and the pass band edge frequency of the left transition band respectively, and  $\omega_{p,right}$  and  $\omega_{s,right}$  are the pass band edge frequency and the stopband edge frequency of the right transition band respectively.

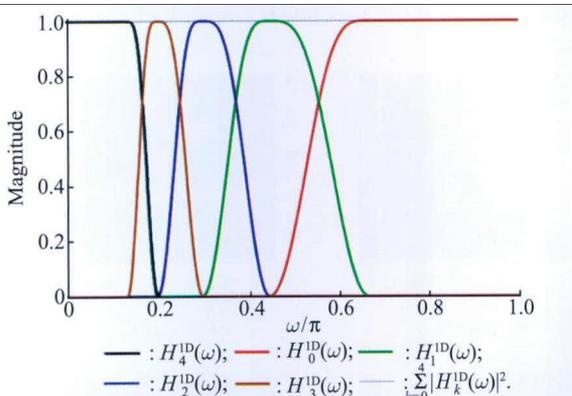


Fig. 7 Frequency response of  $H_j^{1D}(\omega)(j \in \{0,1,2,3\})$  with 4-level decomposition and  $(p, q)=(2, 3)$

If the transition function  $\theta(\omega)$  is chosen such that  $|\theta(\omega)|^2$  is half-band, as the specification in this study, then the passband edges, defined by the half-power frequencies, are the midpoints of the transition bands (12) [19]. The resonant frequency (RF) of  $H_j^{1D}(\omega)$ , defined as the geometric mean of the left and right pass-band edges, is given by (13). Using (12) again, the BW of  $H_j^{1D}(\omega)$  is given by (14). Consequently, we can obtain the Q-factor as (15).

$$RF_j(p, q) = \frac{\pi}{3} \left(1 + \frac{p}{q}\right) \left(\frac{p}{q}\right)^{j-2} \sqrt{\frac{p}{q}}. \quad (13)$$

$$BW_j(p, q) = \frac{\pi}{3} \left(1 + \frac{p}{q}\right) \left(\frac{p}{q}\right)^{j-2} \left(1 - \frac{p}{q}\right). \quad (14)$$

$$Q(p, q) = \frac{RF_j(p, q)}{BW_j(p, q)} = \frac{\sqrt{p/q}}{1 - p/q}. \quad (15)$$

Since  $Q(p, q)$  is constant and independent of the level index  $j$ , our multiscale pyramid employment is a constant-Q transform scheme after  $(p, q)$  parameter is specified in advance. We call the contourlet version based on this multiscale pyramid employment as the tunable-Q contourlet transform because the Q-factor in this version can be flexibly tuned by the  $(p, q)$  parameter. Fig. 8 shows that a higher/lower-Q contourlet version can be achieved by using a  $(p, q)$  parameter with a higher/lower  $p/q$  value.

Using  $H_j(\omega)$  instead of  $L_i(\omega)$  and  $D_i(\omega)$ , the PR condition in (9) can be rewritten as  $\sum_{j=0}^n |H_j(\omega)|^2 = 1$ , for  $n$ -level decomposition. It is pictorially shown in Fig. 7 that the designed  $H_j^{1D}(\omega)$  meets this condition. Of course, the same result will be obtained for their tensor product. In addition, we can see from above that, exactly speaking, the contourlet of Lu is just a particular case with  $(p, q) = (1, 2)$  corresponding to our version.

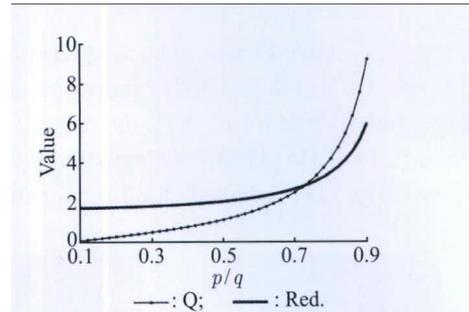


Fig. 8 The Q-factor and Red of the proposed contourlet for various  $(p, q)$  parameters

### 2.5 Redundancy and basis images

As discussed above, the redundancy of the tunable-Q contourlet should also be taken into account. In the following, we calculate its Red defined as the data-quantity ratio of the transform-domain result against the original.

The Red of the structure in Fig. 1 can be inferred easily, as the DFB does not change the data quantity of its input. The Red of  $n$ -level decomposition is presented in (16). As the Red resulted from the nonsampled contourlet version [16] is  $n+1$ , the redundancy from our version is effectively reduced.

$$Red_n(p, q) = 1 + \sum_{j=0}^{n-1} \left(\frac{p}{q}\right)^{2j}. \quad (16)$$

Then, the Red of the tunable-Q contourlet is given by (17).

$$Red(p, q) = \lim_{n \rightarrow \infty} Red_n(p, q) = 1 + \frac{1}{1 - (p/q)^2}. \quad (17)$$

In Fig. 8, we also illustrate the increasing of Red along with the raise of  $p/q$  value.

The basis images of the tunable-Q contourlet in frequency and spatial domain are shown in Fig. 9. Compared with the basis image of the previous contourlet displayed in [14], all the basis images with different  $(p, q)$  parameters here are sharply localized in the desired support area, both in frequency and space domains. Also, we can observe that as the  $p/q$  value or Q-factor rises, the central frequency of the related basis is moving outward obviously.

### 3. Experimental analyses

Using images of different oscillatory nature, we evaluate the effectiveness of the trunable-Q in the proposed contourlet, compared with other transform schemes in applications of image nonlinear approximation (NLA) and denoising.

Various images widely tested in image processing experiments are used here, e.g., Pepper, Tire, Lena and Barbara image. Each of them has a size of  $512 \times 512$ . For

simplicity, the tunable-Q contourlet using the parameter of  $(p, q)$  is denoted as CT  $p/q$ . Other transform schemes include the wavelet transform (WT), the original contourlet transform (CT) of Do [1], and the anti-aliasing contourlet transform of Lu [14] (denoted as CT1/2 for the explana-

tion in Section 2.4). We use four multiscale decomposition levels for all the transforms, and Daubechies 9/7 filters for WT. For the DFB in contourlets, and we use  $(3, 4, 4, 5)$  (the last number 5 corresponds to the finest scale) directional levels for the four levels respectively.

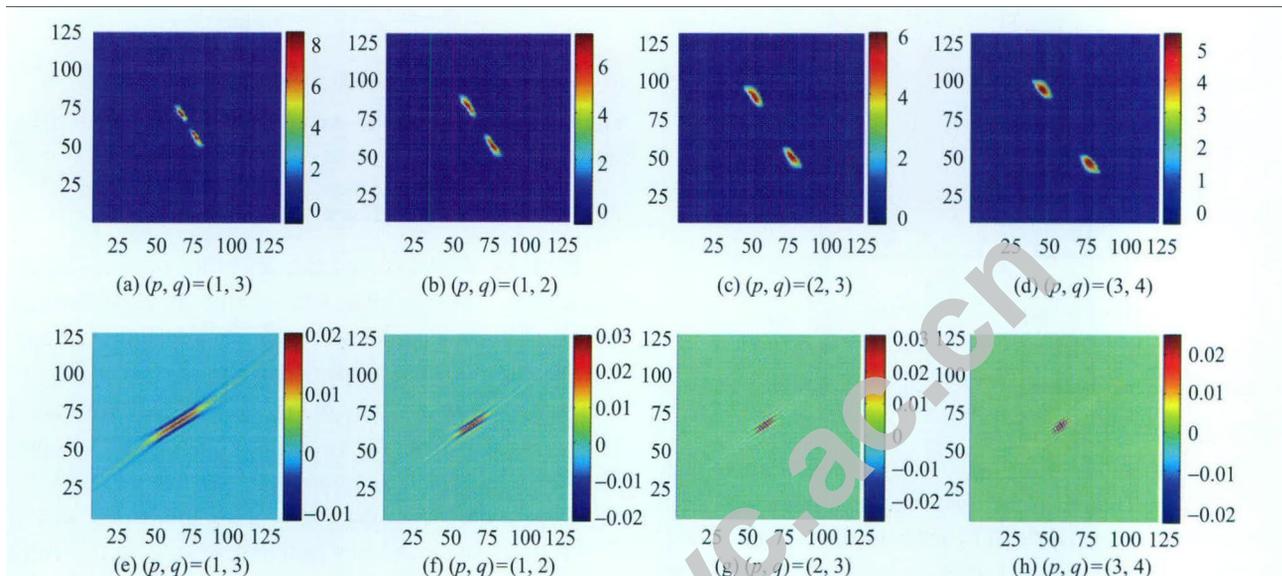


Fig. 9 Images of the contourlet basis with different  $(p, q)$  parameters in frequency (top row) and spatial (bottom row) domains

### 3.1 Nonlinear approximation

To evaluate the NLA performance of each transform scheme, we repeat the experimental idea of Do, i.e., for a given value  $M$ , to select the most significant coefficients in each transform domain, and then to compare the reconstructed images from these sets of  $M$  coefficients in visually quality and in terms of peak signal-to-noise ratio (PSNR) [1]. We expect that most of the refinements happen around the image edges.

We firstly test the NLA results using  $M$  most significant coefficients at the finest scale. Figs. 10 and 11 show the NLA results of two image examples. The proposed contourlet using different  $(p, q)$  parameters show different performance, and the one using a better suitable  $(p, q)$  parameter displays more promising results in capturing edges.

Fig. 12 displays the NLA PSNR results of the two examples versus the number of retained coefficients. The better-suitable  $(p, q)$  parameters consistently provide the contourlet with slightly higher PSNR in different retained numbers.

Then the NLA results using the most significant coefficients at all scales are calculated. Figs. 13 and 14 show a detailed comparison of two NLA results. One can find that

the proposed contourlet using a better-suitable Q-factor preserves better detail structures and avoids more annoying artifacts as well.

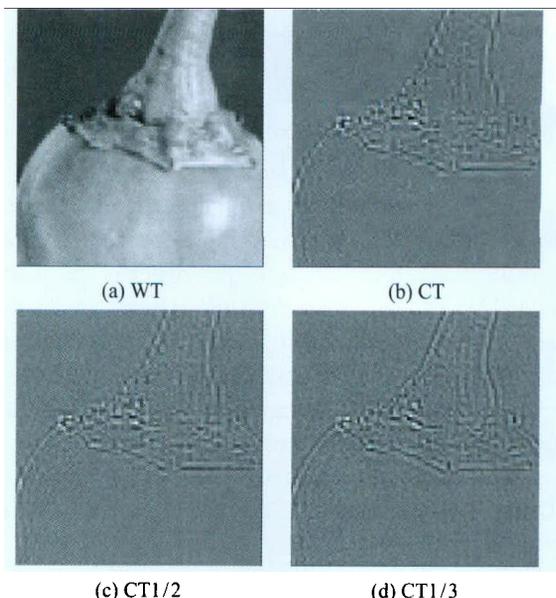


Fig. 10 NLA results of the Pepper image using 4 096 most significant coefficients at the finest scale

Also, Fig. 15 shows the NLA PSNR results of the two images. The proposed transforms consistently gain higher PSNR compared with other transforms too.

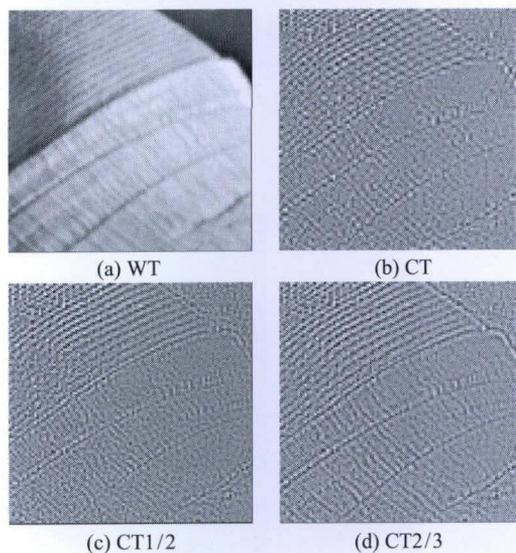


Fig. 11 NLA results of the Lena image using 4 096 most significant coefficients at the finest scale

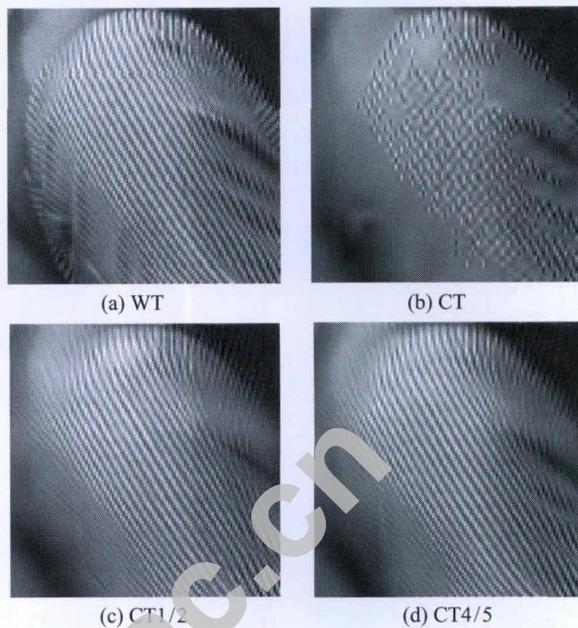


Fig. 14 NLA results of the Barbara image using 16 384 most significant coefficients

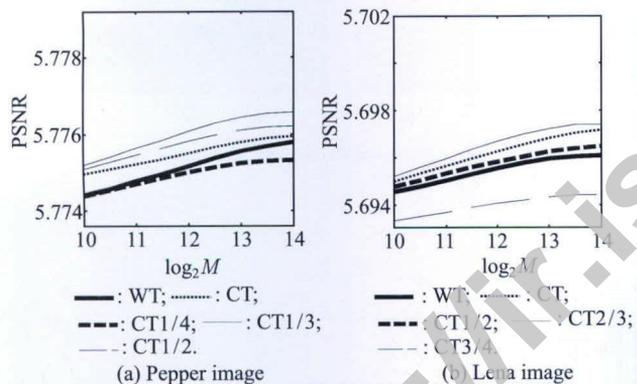


Fig. 12 NLA PSNR results using  $M$  most significant coefficients at the finest detailed subspace

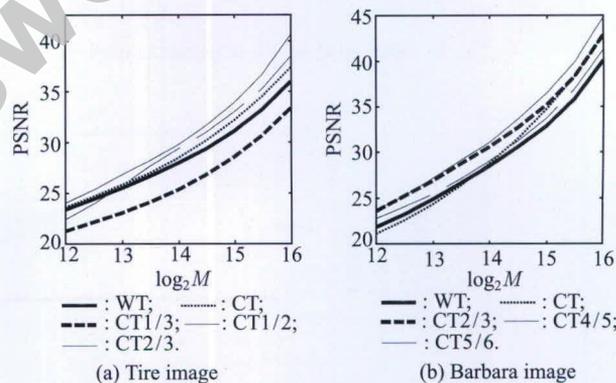


Fig. 15 NLA PSNR result using  $M$  most significant coefficients

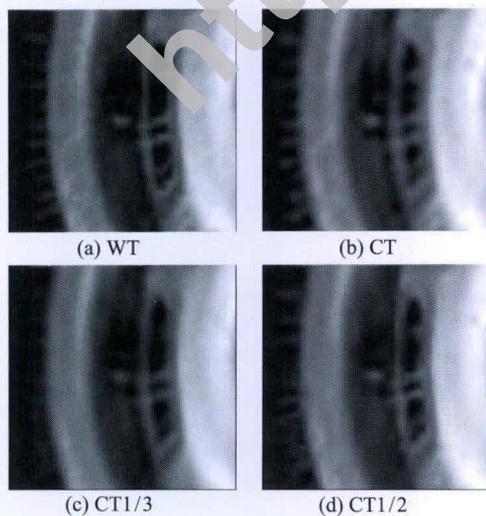


Fig. 13 NLA results of the Tire image using 16 384 most significant coefficients

### 3.2 Image denoising

The improvement in approximation based on keeping the most significant coefficients will directly lead to improvements in applications [1]. In this experiment, we compare the denoising performance of the proposed transform with that of others by using the standard simple hard thresholding rule to shrink the transform coefficients [1,14]. Without the use of more complex shrinkage schemes, we can show the real improvement of the transform.

As examples of the visual results of denoising, in Figs. 16 and 17, we display a “zoom-in” comparison when performing different transform schemes on the Pepper and Lena images. We see that the  $CT_{p/q}$  using a better-suitable parameter retains better edges while results in fewer artifacts compared with other schemes.

To evaluate the different performances of the proposed

transform using various  $(p, q)$  parameters, we display the PSNR values of denoising result corresponding to different  $(p, q)$  parameters in Fig. 18. Also, the PSNR values resulted from the CT and WT are shown here. We can see that for a given image, there is a better-suitable

$(p, q)$  parameter that can yield a more promising denoising result. And by using a better-suitable parameter, the proposed transform can outperform wavelets and the previous contourlets in denoising.

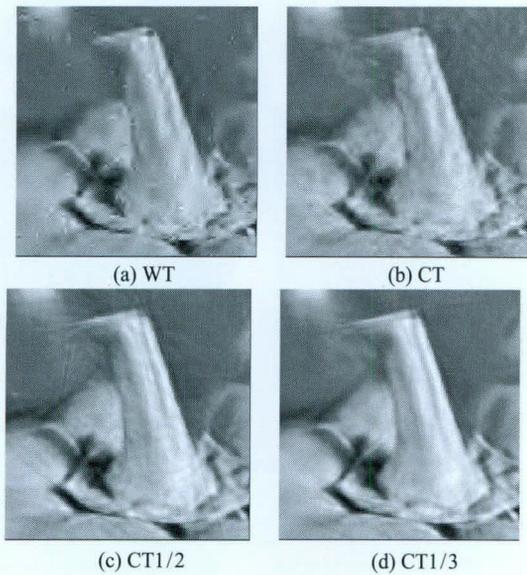


Fig. 16 Denoising results of Peppers image

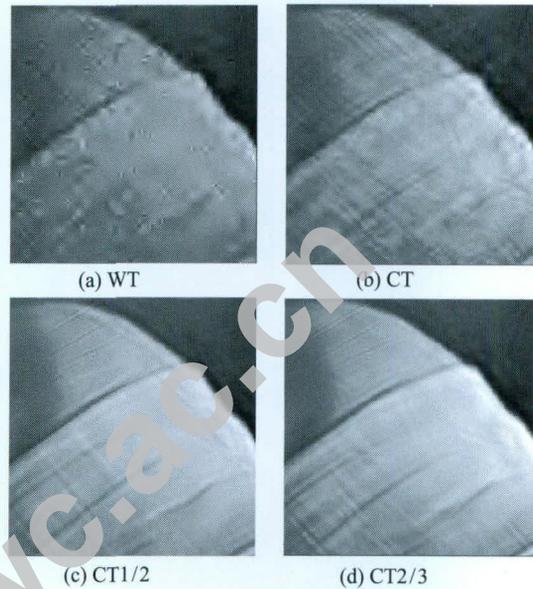


Fig. 17 Denoising results of Lena image

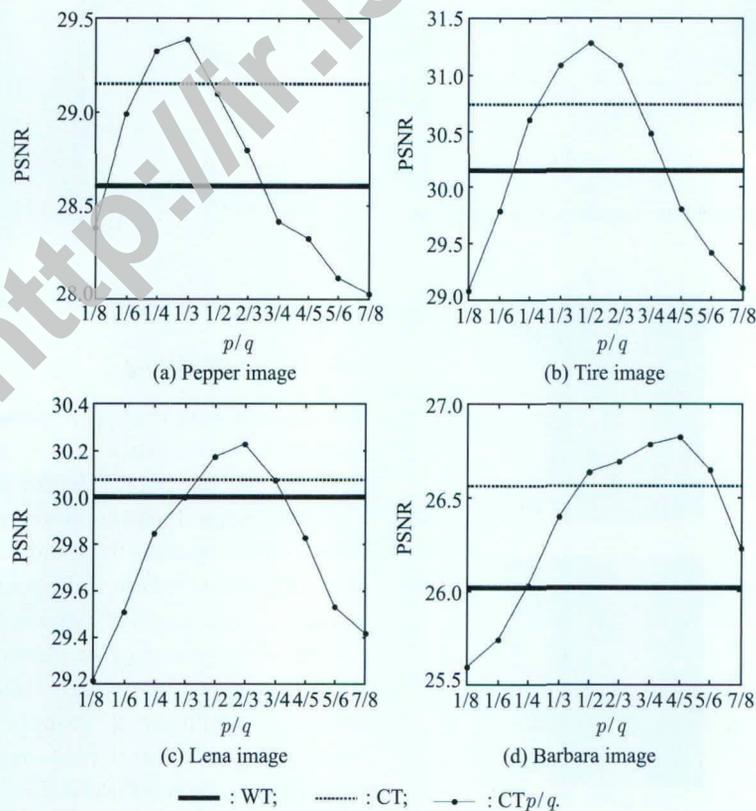


Fig. 18 PSNR of denoising results versus different  $(p, q)$  parameters

### 3.3 Computational complexity

An effective image representation scheme should incur reasonable computational complexity. The computational time generally required by the proposed contourlet is analyzed in the followings, compared with those required by WT and CT. The computation spans from the start of the decomposition to the end of the reconstruction for each transform scheme. The parameters about the multiscale level of all the schemes, the directional level of DFB and the filter of WT are similarly used as above. For the  $(p, q)$  parameter of  $CT_{p/q}$ , various cases usually adopted are tested. We perform each transform scheme on images with different dataset sizes. For each size level of each transform scheme, the time spans corresponding to different images with this size are counted respectively, and then the mean of these time spans is taken as an actual computational time generally required by the scheme for this size level. We use the following standard tested images—Pepper, Tire, Lena and Barbara, and linearly interpolate each image in the experiment when requiring its counterpart with other dataset size.

All the transform schemes are realized with Matlab software, with the WT code supported by this software and the CT code provided by Do [1]. The computer equipment

used is the same for all the transform schemes: Pentium 4 central processor with 2.80 GHz and a memory with 1 GB capacity.

The experimental results are reported in Table 1. We also pictorially show the results corresponding to the size level of  $1\ 024 \times 1\ 024$  in Fig. 19. For each size level, the computational time required by  $CT_{p/q}$  with every  $(p, q)$  parameter is more than that of WT; while it is close to that of CT although comparatively a little more. Also, for each  $(p, q)$  parameter case, the time required by  $CT_{p/q}$  and CT is still close even when the dataset size reaches up to  $1\ 024 \times 1\ 024$ , as pictorially shown in Fig. 19. It indicates that the computational complexity of  $CT_{p/q}$  is generally close to that of CT. The  $CT_{p/q}$  incurs reasonable computational complexity mainly because the processes of its multiscale filtering and resampling in Fig. 1 are all efficiently realized in frequency domain (The processes are similar to those of [19]).

Also, Table 1 shows that for each size level, as the value of  $p/q$  gradually increases or decreases, the computational time required by  $CT_{p/q}$  rapidly converges toward certain acceptable value after a little increase. Fig. 19 obviously illustrates its convergence trend. It indicates that the proposed contourlet with other lower or higher Q-factors is still an efficient image representation scheme.

Table 1 Computational time required by different transform schemes

Dataset size	Transform scheme											
	WT	CT	CT1/8	CT1/6	CT1/4	CT1/3	CT1/2	CT2/3	CT3/4	CT4/5	CT5/6	CT7/8
256×256	0.167	0.505	0.535	0.534	0.532	0.524	0.516	0.529	0.538	0.544	0.547	0.548
512×512	0.637	1.827	1.972	1.970	1.967	1.956	1.940	1.969	1.982	1.989	1.993	1.996
1 204×1 204	2.317	7.112	7.575	7.568	7.549	7.464	7.312	7.451	7.664	7.731	7.757	7.766

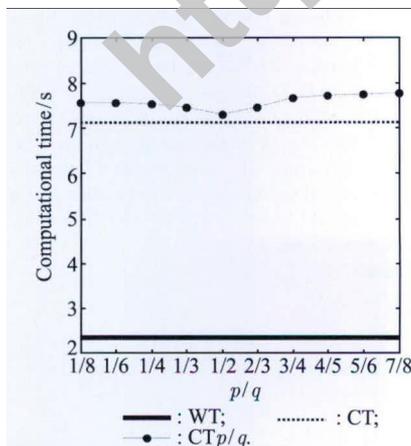


Fig. 19 Computational time required by WT, CT and  $CT_{p/q}$  with various  $(p, q)$  parameters

### 4. Conclusions

A new tunable-Q contourlet transform for representing im-

ages of different oscillatory nature is proposed in this paper. This transform provides a tunable parameter  $(p, q)$  by which one can flexibly tune the Q-factor of the proposed contourlet. By directly designing the multiscale FB in frequency domain, the aliasing component in the DFB of the original contourlet is effectively reduced. We use the transform in nonlinear approximation and image denoising. The result shows that the contourlets using different  $(p, q)$  parameters result in different performances, and the one using a better-suitable  $(p, q)$  parameter preserves more detail edges while generates less annoying artifacts compared with that of wavelets and the previous contourlets.

We should use the better-suitable Q-factor when we apply the tunable-Q contourlet to a given image. The subsequent issue is how to chose the most suitable  $(p, q)$  parameter for a particular image, and we leave it to our future work.

## Acknowledgements

The authors would like to thank Bayram Iker of Polytechnic Institute of New York University, and Shouzhi Yang of Department of Mathematics, Shantou University, China, for many useful questions and comments.

## References

- [1] M. N. Do, M. Vetterli. The contourlet transform: an efficient directional multiresolution image representation. *IEEE Trans. on Image Processing*, 2005, 14(12): 2091–2106.
- [2] S. F. Ma, G. F. Zheng, L. X. Jin, et al. Directional multiscale edge detection using the contourlet transform. *Proc. of the 2nd IEEE International Conference on Advanced Computer Control*, 2010: 58–62.
- [3] K. Liu, L. Guo, J. S. Chen. Contourlet transform for image fusion using cycle spinning. *Journal of Systems Engineering and Electronics*, 2011, 22(2): 353–357.
- [4] Y. H. Fan, G. Wang, X. Liang. A static image coding algorithm based on contourlet classified hidden Markov tree model. *Engineering Computations*, 2011, 28(1/2): 172–183.
- [5] Y. Yang, Q. Dai. Contourlet-based image quality assessment for synthesised virtual image. *Electronics Letters*, 2010, 46(7): 492–493.
- [6] G. S. Hu, D. Liang, L. S. Huang. Remote sensing image denoising based on support vector value contourlet transform. *Systems Engineering and Electronics*, 2011, 33(7): 1658–1663. (in Chinese)
- [7] Y. B. Sun, X. Fei, Z. H. Wei, et al. Image perceptual quality assessment using contourlet transform. *Acta Electronica Sinica*, 2010, 39(3): 649–655. (in Chinese)
- [8] N. G. Chitaliya, A. I. Trivedi. An efficient method for face feature extraction and recognition based on contourlet transforms and principal component analysis. *Proc. of the International Conference and Exhibition on Biometrics Technology*, 2010: 52–61.
- [9] Y. S. Dong, J. W. Ma. Contourlet-based texture classification with product bernoulli distributions. *Proc. of the 8th International Symposium on Neural Networks*, 2011: 9–18.
- [10] I. Daubechies. *Ten lectures on wavelets*. Philadelphia: Society for Industrial and Applied Mathematics, 1992.
- [11] I. W. Selesnick. Wavelet transform with tunable Q-factor. *IEEE Trans. on Signal Processing*, 2011, 59(8): 3560–3575.
- [12] Y. L. Qiao, C. Y. Song, C. H. Zhao. M-band ridgelet transform based texture classification. *Pattern Recognition Letters*, 2010, 31(3): 244–249.
- [13] I. W. Selesnick. Sparse signal representations using the tunable Q-factor wavelet transform. *Proc. of the International Society for Optical Engineering*, 2011: 8138U.
- [14] Y. Lu, M. N. Do. A new contourlet transform with sharp frequency localization. *Proc. of the IEEE International Conference on Image Processing*, 2006: 1629–1632.
- [15] N. Mueller, Y. Lu, M. N. Do. Image interpolation using mul-

tiscale geometric representations. *Proc. of the International Society for Optical Engineering*, 2007: 64980A.

- [16] L. Cunha, J. P. Zhou, M. N. Do. The nonsubsampling contourlet transform theory design and application. *IEEE Trans. on Image Processing*, 2006, 15(10): 3089–3101.
- [17] P. P. Vaidyanathan. *Multirate systems and filter banks*. Englewood Cliffs, NJ: Prentice-Hall, 1993.
- [18] R. H. Bamberger, M. J. T. Smith. A filter bank for the directional decomposition of images: theory and design. *IEEE Trans. on Signal Processing*, 1992, 40(4): 882–893.
- [19] I. Bayram, I. W. Selesnick. Frequency-domain design of over-complete rational-dilation wavelet transforms. *IEEE Trans. on Signal Processing*, 2009, 57(8): 2957–2972.

## Biographies



**Haijiang Wang** was born in 1979. He received his B.S. degree from Hebei Normal University in 2005 and M.S. degree from Ludong University in 2009. He is now a Ph.D. candidate in Institute of Soil and Water Conservation, Chinese Academy of Sciences and Ministry of Water Resources. His main research interest includes image processing methods and their applications.

E-mail: wanghaijiang\_study@126.com



**Qinke Yang** was born in 1966. He is currently a professor in Northwest University, and also a professor in Institute of Soil and Water Conservation, Chinese Academy of Sciences and Ministry of Water Resources. His main research interest includes applications of image processing methods to DEM multiscale representation.

E-mail: qkyang@nwu.edu.cn



**Rui Li** was born in 1946. He is currently a professor in Institute of Soil and Water Conservation, Chinese Academy of Sciences and Ministry of Water Resources, and also a professor in Northwest A&F University. His main research interest includes applications of image processing methods to DEM multiscale representation.

E-mail: ruili@nwsuaf.edu.cn



**Zhihong Yao** was born in 1970. She is currently a lecturer in North China University of Water Resources and Electric Power. She received her M.S. and Ph.D. degrees in Institute of Soil and Water Conservation, Chinese Academy of Sciences and Ministry of Water Resources in 2007 and 2012, respectively. Her main research interest includes regional soil and water conservation and applications of GIS.

E-mail: yaozhihong@ncwu.edu.cn